

On the Variability in the Onset of the Norwegian Coastal Current

KAI HÅKON CHRISTENSEN

Norwegian Meteorological Institute, and University of Oslo, Oslo, Norway

ANN KRISTIN SPERREVIK

Norwegian Meteorological Institute, Oslo, Norway

GÖRAN BROSTRÖM

University of Gothenburg, Gothenburg, Sweden

(Manuscript received 14 June 2017, in final form 22 November 2017)

ABSTRACT

A high-resolution reanalysis of the circulation in the Kattegat and Skagerrak is used to investigate the mechanisms that control the variability in the onset of the Norwegian Coastal Current. In the reanalysis, the authors have used all available in situ and remote sensing observations of salinity and temperature and use surface current observations from two coastal high-frequency radars that were ideally placed to monitor the exchange between the two basins. This study finds a strong correlation between the variability in the wind forcing in the Skagerrak and the transport in the Norwegian Coastal Current through the Torungen–Hirtshals section. Two cases with winds into and out of the Skagerrak are studied in more detail, and the results suggest asymmetries in the forcing mechanisms. For winds out of the Skagerrak, strong outflows of Baltic Sea Water associated with a deflection of the Kattegat–Skagerrak Front may disrupt local processes in the Skagerrak, which is not accounted for in previously published conceptual models for the variability of the coastal currents in this region.


1. Introduction

The Kattegat and Skagerrak connect the Baltic Sea and North Sea. Here, three water masses meet: Baltic Sea Water coming through the sounds in the south, North Sea Water carried with the Jutland current along the Danish west coast, and subsurface Atlantic Water (AW) branching off the Atlantic Current north of Scotland and flowing south along the coast of Norway (see Fig. 1). The Jutland and Baltic currents converge outside the northern tip of Denmark, Skagen, forming the Kattegat–Skagerrak Front.

The ship traffic in the region is heavy, with approximately 40 000–60 000 larger vessels passing through

every year, and major oil spills in recent years have been caused by groundings or ship collisions (e.g., Broström et al. 2011). There are hundreds of shipwrecks in the region, containing bunker oil, mustard gas, white phosphorous and other hazardous loads, and leakage of toxic material from sunken vessels poses another environmental hazard. In addition, there are hundreds of thousands of pleasure crafts in the region, the use of which peaks strongly in the summer months. Operational circulation models are thus needed both for ship routing, oil spill drift models, and for search and rescue support. The circulation in the Kattegat–Skagerrak is challenging to model, however, and multimodel ensembles show large differences between modeling systems (Golbeck et al. 2015).

Of particular interest is the onset of the Norwegian Coastal Current (NCC), since the NCC influences the environmental conditions along the entire Norwegian coast. The NCC originates in the Skagerrak as a continuation of the Baltic Sea outflow (BO), and it flows along the Norwegian coast all the way up into the

 Denotes content that is immediately available upon publication as open access.

Corresponding author: Kai H. Christensen, kai.h.christensen@met.no

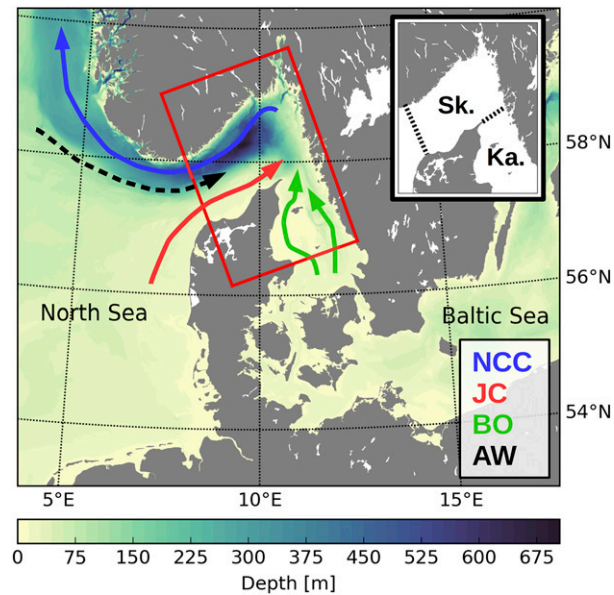


FIG. 1. Lateral boundaries of the model (red) as well as the main currents in the Kattogat–Skagerrak system: the NCC (blue), JC (red), BO (green), and Dooley Current with AW (black). The inset shows the approximate boundaries of the Kattegat and Skagerrak.

Barents Sea. It carries freshwater from the Baltic Sea and the Norwegian rivers into the Arctic and hence plays an important role in the Arctic freshwater budget. Along most of the Norwegian coast, the cold and fresh NCC is wedged between the warm and saline Norwegian Atlantic Current and the coast, and mixing between the Atlantic and coastal waters gradually reduce the contrast between the two water masses as they flow northward. Typical current speeds in the NCC are about 0.25 m s^{-1} but occasionally exceed 1 m s^{-1} (Aure et al. 2007). There is a seasonal variation in the NCC: in the summer it is wide and shallow, while in the winter it turns narrow and deep. From a climate perspective there is a trend toward increasing temperatures in the NCC of the order of 1°C (average in the years 2000–09 compared to the average for 1961–90; see Albretsen et al. 2012).

In this paper we use a 14-month-long reanalysis of the Kattogat–Skagerrak circulation to investigate the variability in the onset of the NCC and the causes for this variability. Our focus is on the response to the large-scale wind forcing in the Skagerrak, which is associated with Ekman transport across the Skagerrak and upwelling and downwelling along the Norwegian and Danish coasts. We use the four-dimensional variational data assimilation (4D-Var) analysis scheme in the Regional Ocean Modeling System (ROMS), assimilating satellite sea surface temperature and in situ salinity and temperature from a variety of sources. The observations also include data from two high-frequency (HF) coastal

radars that were temporarily deployed just north of the Kattogat–Skagerrak front, hence providing an excellent constraint on the exchange between the two basins. In 4D-Var, tangent linear and adjoint model components are used to propagate the model–observation differences (innovations) back and forth in time, and hence the model physics provide multivariate correlations between observed and unobserved variables.

Previous observation and modeling studies have focused on integrated parameters such as freshwater height and available potential energy, linking these quantities to the circulation (e.g., Gustafsson and Stigebrandt 1996; Røed and Albretsen 2007). We do not rely on such integrated parameters to estimate the currents as these are taken directly from the model, although we use the freshwater height and the potential energy to investigate the time development of the surface layer for different surface forcing conditions.

The outline of the paper is as follows: In section 2 we briefly describe the main features of the circulation in the Kattogat–Skagerrak. In section 3, we describe the modeling system and the observations that we use to produce our reanalysis. In section 4, we present the results from the reanalysis, focusing on the components of the overall circulation that have a major influence on the NCC. Finally, section 5 contains a discussion and some concluding remarks.

2. The circulation in the Kattogat–Skagerrak

The Kattogat and Skagerrak Basins are mostly shallow, with the exception of the Norwegian Trench, which extends from the Norwegian Sea and follows the coastline into the Skagerrak (Fig. 1). The northern part of the Skagerrak is therefore the deepest, with a maximum depth of 710 m. The southern part toward Denmark is much shallower, with depths decreasing slowly from about 50 m in the central part of the basin to the sandy northern coastline of Denmark. The Norwegian Trench continues as the Deep Trench into the Kattogat along the Swedish coast, with depths slowly decreasing from about 100 m in northern Kattogat to the Belt Sea and Öresund in the south. Here, the Kattogat connects to the Baltic Sea through narrow straits and the main flows are over the Darss Sill (18 m) and the Drogden Sill (8 m). The tides are dominated by the semidiurnal component, and the tidal range is small in both basins (typical offshore range is 5–10 cm). The largest rivers that flow into the Kattogat and Skagerrak are Glomma, Drammenselva, and Göta Älv (see Fig. 2), with average discharges in the years 2014–15 of 853, 448, and $604 \text{ m}^3 \text{ s}^{-1}$, respectively (data from the national hydrological services).

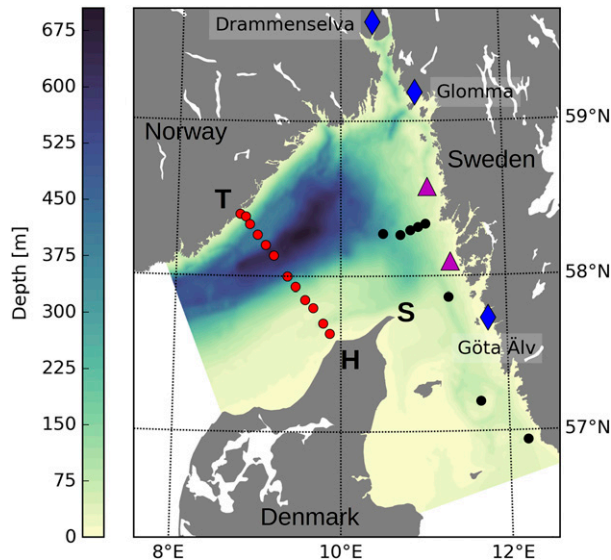


FIG. 2. Location of the three largest rivers Glomma, Göta Älv, and Drammenselva (diamonds). Also shown are the locations of the two HF radars (triangles) at Måseskär (southernmost) and Väderöarna. The range of these HF radars was approximately equivalent to the distance from the Swedish coast to the tip of Denmark at Skagen (S). The black dots show hydrographic stations that are part of regular Swedish monitoring cruises, while the red dots show the stations on the Torungen–Hirtshals section.

The outflow from the Baltic Sea has been shown to correlate well with large-scale gradients in mean sea level pressure (Stigebrandt 1983) but is out of phase with the freshwater supply to the Baltic Sea (Aure et al. 2007). The response to the weather systems can be very strong in the Danish straits, with barotropic flows exceeding the freshwater flow out of the Baltic Sea by one order of magnitude (Stigebrandt 1983). The Kattegat is well represented as a two-layer system, with the surface layer increasing in salinity from about 10–12 in the south to about 20–25 toward the Kattegat–Skagerrak Front, and below the surface layer we find Skagerrak water with salinities between 30 and 35 (e.g., Stigebrandt 1983; Gustafsson 1997; Jakobsen 1997). The overall circulation in the surface layer is anticyclonic with variations caused by changes in the Baltic Sea outflow and the position of the Kattegat–Skagerrak Front (Stigebrandt 1987; McClimans et al. 2000; Nielsen 2005).

In the Skagerrak the surface circulation is primarily cyclonic, and the sea surface height has its minimum in the central part of the basin. The NCC flows westward out of the Skagerrak on the northern side while the Jutland Current (JC) brings North Sea Water influenced by the discharge from major rivers in the southern part of the North Sea (i.e., the Rhine, Meuse, and Elbe). The so-called Dooley Current (Dooley 1974) brings Atlantic

Water in from the northern North Sea along the southern rim of the Norwegian Trench, and this water forms the bottom layer. The surface layer is thinnest in the central part of the Skagerrak where the Atlantic Water often can be found at 10–20-m depth (e.g., Gustafsson and Stigebrandt 1996). There is a seasonal variability in freshwater height in the Skagerrak, which on average is related to the seasonal variability in the Baltic Sea outflow (Gustafsson and Stigebrandt 1996; Aure et al. 2007). The response to local wind forcing is complex, and Ekman transport across the central part of the Skagerrak contributes to exchange between the NCC and JC, and also influences the exchange between the Skagerrak and the Kattegat (e.g., Danielssen et al. 1997).

The transport out of the Kattegat and into the Skagerrak has been estimated to be between $45\,000\text{--}80\,000\text{ m}^3\text{ s}^{-1}$, and the average outflow from the Skagerrak in the NCC has been estimated to $400\,000\text{ m}^3\text{ s}^{-1}$ (Gustafsson 1997). The difference between these two transports is due to the JC and Dooley Current (see Fig. 1). Thus, the Baltic Sea outflow is only a small part of the total transport in the NCC, and there is considerable mixing of the various water masses in the Skagerrak. Extensive field campaigns were launched in 1990–91 (SKAGEX; see, e.g., Berntsen and Svendsen 1999, and references therein), which provided near-synoptic hydrographic data for extended periods. Analysis of the SKAGEX dataset has indicated that the coastal currents are strongly correlated with the local wind forcing, with a response time of about one week (Gustafsson 1999). This response time is consistent with a baroclinic signal propagating with a speed of about 1 m s^{-1} around the rim of the Skagerrak Basin.

3. Methods

a. Ocean circulation model

We use ROMS, which is a primitive equation model with split-explicit time stepping, and that uses topography-following vertical coordinates (Shchepetkin and McWilliams 2005, 2009). The model domain is indicated in Fig. 1. The horizontal resolution is approximately 1 km, and we use 50 vertical layers. The minimum depth in the model is set to 10 m. The quadratic bottom friction coefficient is increased in shallow areas both for reasons of numerical stability and also to reduce the flow in the regions where the actual depth is less than the model minimum depth. Vertical mixing is parameterized using the two-equation $k\text{--}\omega$ scheme (Umlauf et al. 2003; Warner et al. 2005), with surface

wave breaking as a source of turbulent kinetic energy parameterized as in [Craig and Banner \(1994\)](#). The model has been spun up from 1 January 2014, with 4D-Var data assimilation from 1 September 2014. We show results here for the period 1 October 2014 to 30 November 2015.

The model is forced with hourly data from the numerical weather prediction model Applications of Research to Operations at Mesoscale (AROME)–Meteorological Cooperation on Operational Numerical Weather Prediction (MetCoOp) of the Norwegian Meteorological Institute and the Swedish Hydrological and Meteorological Institute (SMHI). This model has a horizontal resolution of 2.5 km. Surface fluxes are obtained via the COARE3.0 bulk flux algorithms ([Fairall et al. 2003](#)) that are built into ROMS. The lateral boundary conditions are obtained from the operational Baltic and northwest shelf ocean model components of the Copernicus Marine Environment Monitoring Service (see <http://marine.copernicus.eu>; the data streams are BALTICSEA_ANALYSIS_FORECAST_PHYS_003_006-TDS and NORTHWESTSHELF_ANALYSIS_FORECAST_PHYS_004_001_b, respectively). These model fields are averaged to provide daily inputs, interpolated to our native model grid to provide model values in boundary relaxation zones toward the North Sea and the Baltic Sea, respectively. The matching to exterior values is implemented as in [Marchesiello et al. \(2001\)](#) with a mixture of nudging and radiation conditions. The model is also forced with seven tidal components from the TPXO global inverse barotropic model ([Egbert and Erofeeva 2002](#)). Freshwater discharge from 38 rivers are provided as daily climatological values, except for the three largest rivers (Glomma, Drammenselva, and Göta Älv) for which we provide daily averages obtained from Norwegian and Swedish authorities.

b. Analysis scheme

We use the 4D-Var analysis scheme implemented in ROMS (ROMS–4DVAR; [Moore et al. 2011a,b,c](#)). More specifically, we use the Physical-Space Statistical Analysis System (PSAS) with the restricted preconditioned conjugate gradient (RPCG) algorithm of [Gratton and Tshimanga \(2009\)](#) and a 24-h assimilation window. It is possible to include the surface fluxes and lateral boundary conditions in the control variable vector of ROMS–4DVAR, and this has been done here. The background error variances needed for ROMS–4DVAR are assumed to be equal to the variances of the corresponding variables in a free model run covering the same period as the reanalysis (e.g., [Broquet et al. 2009](#)). Univariate error covariances are modeled using a diffusion operator ([Weaver and Courtier 2001](#); [Moore et al. 2011a](#)), and the horizontal and vertical

decorrelation scales are taken to be 10 km and 20 m, respectively. No balance relations between control variables have been used for explicit multivariate error covariances. Examination of the ROMS–4DVAR output (i.e., the linear and nonlinear cost function values) indicates that the assumption of linear dynamics within the 24-h assimilation window is reasonable (e.g., [Neveu et al. 2016](#), not shown here).

c. Observations

In situ observations of temperature and salinity were collected from three different sources: the Copernicus Marine Environment Monitoring Service (see <http://marine.copernicus.eu>), the EN4 dataset available from the Met Office ([Good et al. 2013](#)), and from the International Council for the Exploration of the Sea (see <http://ocean.ices.dk>). The compiled dataset consists of observations from a variety of observational platforms, such as monitoring cruises, FerryBox ([Haller et al. 2015](#)), and moorings. The sea surface temperature (SST) data are from individual satellite overpasses projected onto a grid with 1.5-km resolution ([Eastwood 2011](#)). The SST data used here are obtained from infrared sensors and thus observations are only available during cloud-free conditions.

The SMHI deployed medium-range (13.5 MHz) CODAR SeaSonde HF radars late in 2014 on two sites on the Swedish west coast at Måseskär and Väderöarna (see [Fig. 2](#)). The radars were operative throughout 2015, but changes in carrier frequency and bandwidth were made in winter/spring 2015 because of issues with signal to noise ratios. For this reason we only use HF radar data collected from 1 April 2015. The combined data (total vectors) from the two sites were assimilated as horizontal velocity vectors with an effective depth of 0.7 m ([Röhrs et al. 2015](#)).

d. Transports, wind forcing, freshwater height, and profile potential energy

For the analysis of the NCC variability we calculate the transports through the section Torungen–Hirtshals ([Fig. 2](#)). The model results show that, on average, neither the NCC or the JC extend across the deepest point of the Norwegian Trench, and the NCC and JC transport estimates are calculated for the subsections indicated in [Fig. 8](#) (shown below). In addition, the NCC is usually confined to the upper 200 m (e.g., [Aure et al. 2007](#)); hence, we do not include the transport below this depth to reduce the influence of the subsurface Atlantic Water in the Norwegian Trench. The changes in the modeled NCC transport caused by assimilating the various observation types are discussed later on in [section 4b](#).

We also calculate the time-integrated wind stress τ in the direction \mathbf{n} normal to the Torungen–Hirtshals section as

TABLE 1. Verification statistics: biases and RMSE.

	Posterior bias	Prior bias	Posterior RMSE	Prior RMSE
u (native) (m s^{-1})	-0.006	0.000	0.168	0.225
v (native) (m s^{-1})	-0.007	0.052	0.195	0.255
Temperature (K)	0.006	-0.079	0.552	0.767
Salinity	-0.028	-0.057	0.873	0.981

$$\overline{\tau}(t) = \frac{1}{T} \int_{-T+t}^t [\overline{\tau}_A(t') \cdot \mathbf{n}] dt', \quad (1)$$

where the overbar denotes the spatial average of the model wind stress τ_A in the region indicated in Fig. 8. In section 4d, we correlate this average wind stress with the modeled NCC and JC transports, and the time period T is varied in order to identify the response time of the coastal currents to changes in the wind forcing. This method is closely related to that of Austin and Barth (2002), who investigated upwelling along the coast of Oregon. Instead of using a fixed averaging period, Austin and Barth (2002) assumed an exponential decay

associated with a relaxation time scale based on theory for damped coastal jets.

To investigate the transport of freshwater in the surface layer we calculate the freshwater height from the salinity S as

$$\text{FWH} = \int_{\zeta-10}^{\zeta} \frac{\max(0, 35 - S)}{35} dz, \quad (2)$$

where ζ is the instantaneous sea surface height. For comparison with other studies utilizing the freshwater height (e.g., Gustafsson and Stigebrandt 1996; Gustafsson 1999), please note that we restrict the integration to the

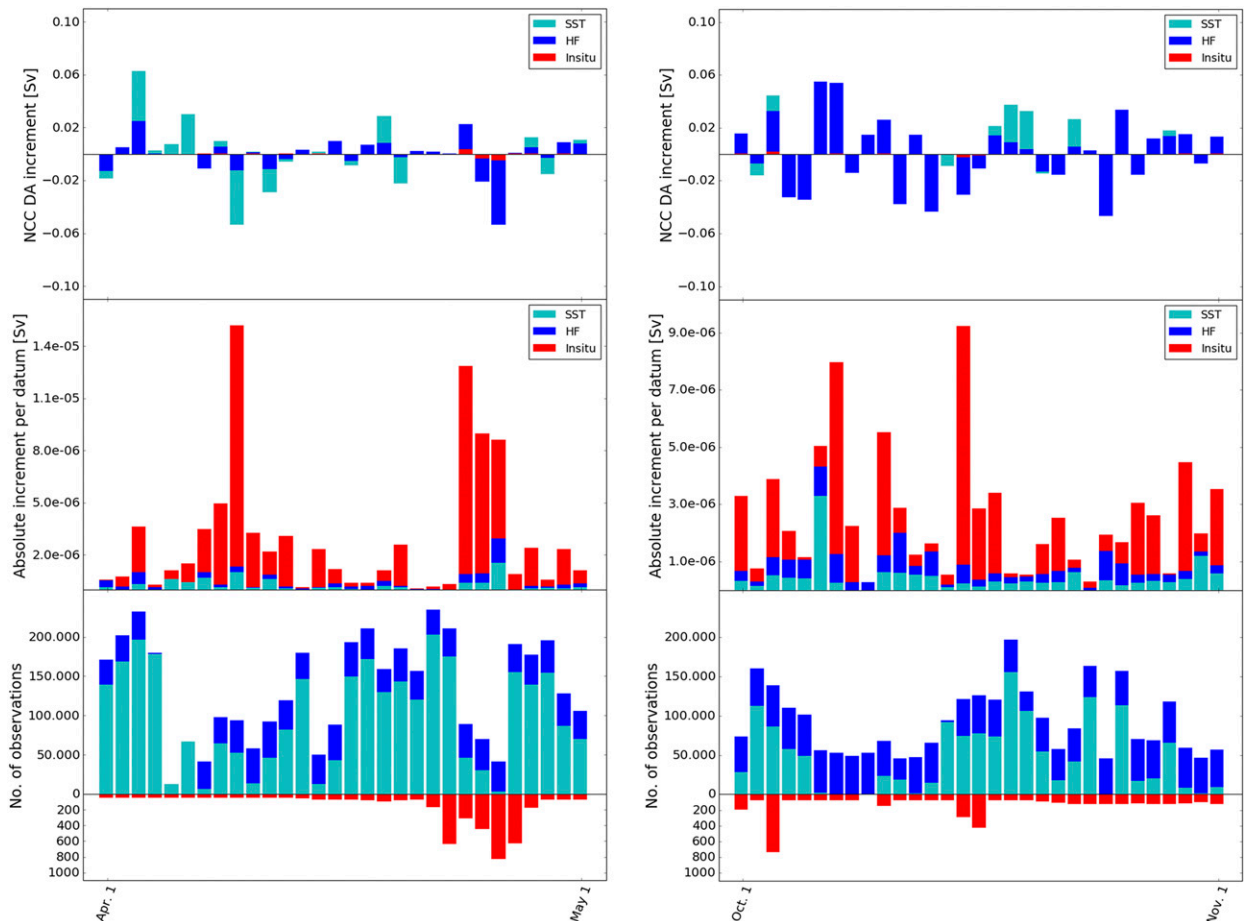


FIG. 3. (top) Impact of the observations on the analysis increment in the NCC in (left) April and (right) October 2015. Each bar represents one assimilation cycle of 24 h. (middle) Average impact per observation (absolute value). (bottom) Number of observations per assimilation cycle. All values are positive, and the axis is reversed for the in situ data to emphasize the difference in scale.

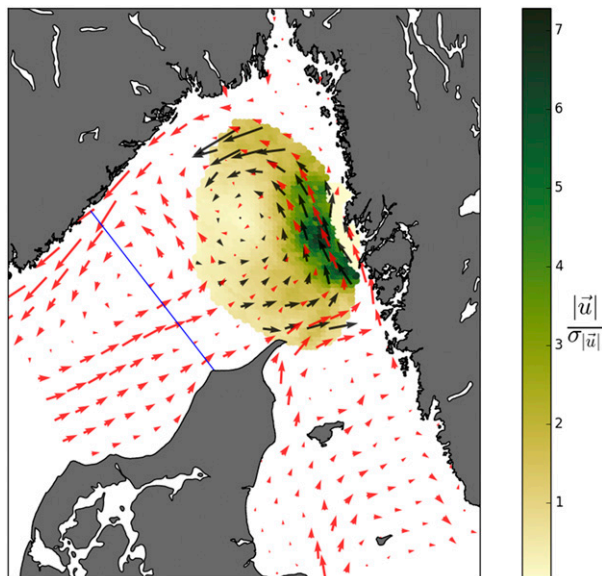


FIG. 4. Average HF radar currents (black) and model currents (red) for the period 1 Apr to 26 Oct 2015. The filled contours show the average HF radar speed divided by the average estimated observation error. Note that the zonal components of the HF radar currents near the southern and northern ends of the coverage area are associated with large errors because of the so-called geometrical dilution of precision (see [Chapman and Graber 1997](#)). The straight line across the Skagerrak in this and the following figures shows the Torungen–Hirtshals section.

upper 10 m of the water column to avoid excessive influence of bathymetry on the results.

Finally, we also consider the profile potential energy, which is the excess potential energy in a stratified water column as compared to one with uniform density. It is defined as

$$\text{PPE} = -\frac{g}{\rho_0} \int_{-D}^{\zeta} \max(\rho_0 - \rho, 0) z \, dz, \quad (3)$$

where D is the depth and ρ_0 is the reference density chosen by [Gustafsson \(1999\)](#) based on a salinity of 35 and a temperature of 8°C, representative of the Atlantic Water masses found in our region of interest.

The freshwater height and profile potential energy can be used to approximate streamfunctions for geostrophic surface currents and vertically integrated transports, respectively, and have therefore been used in previous studies of the dynamics in the Kattegat and Skagerrak (e.g., [Stigebrandt 1987](#); [Gustafsson and Stigebrandt 1996](#); [Gustafsson 1999](#))

4. Results

a. Verification

Average prior and posterior model error statistics for the period 1 October 2014 to 30 November 2015 are

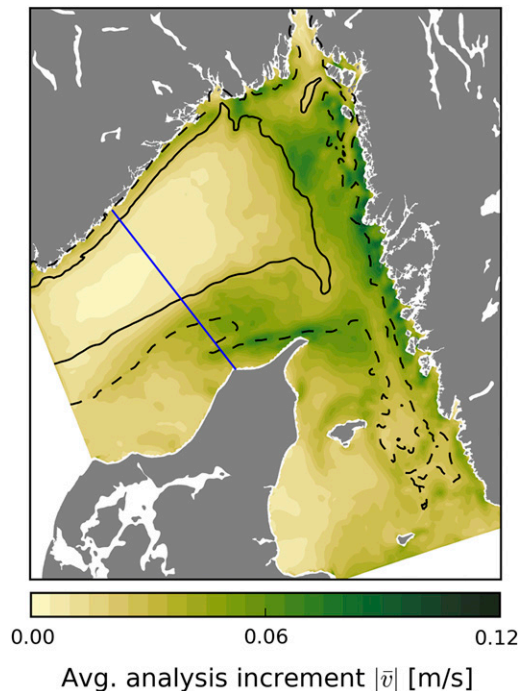


FIG. 5. Average analysis increment in the vertically averaged current speeds (1 Apr to 31 Oct 2015). The isolines denote the 200-m (solid) and 50-m isobaths (dashed).

shown in [Table 1](#). The posterior biases are reduced compared to the prior biases, demonstrating that the analysis scheme successfully draws the model closer to the observations. The only exception is the native u -velocity component, which has a negligible bias from the outset. The HF radar observations are taken at a location where the native u velocities are more or less normal to the coastline and thus close to zero; hence, a small bias for this variable is not surprising. The biases are in general small, which is encouraging since the analysis scheme assumes a bias-free model, although that is difficult to achieve in practice. The posterior root-mean-square errors (RMSE) are smaller than the prior RMSE for all state variables. We may note here that many of the salinity observations are from a mooring close to the Swedish coast where we would expect the model to be less accurate because of unresolved processes. If these observations are left out, the prior and posterior RMSE values for salinity become 1.031 and 0.655, respectively, which should be more representative for observations collected by research vessels, drifting buoys, FerryBox, and other instrument platforms operating farther offshore.

b. Observation impacts

Analysis increments are defined as the analysis minus the background, that is, the differences in model values

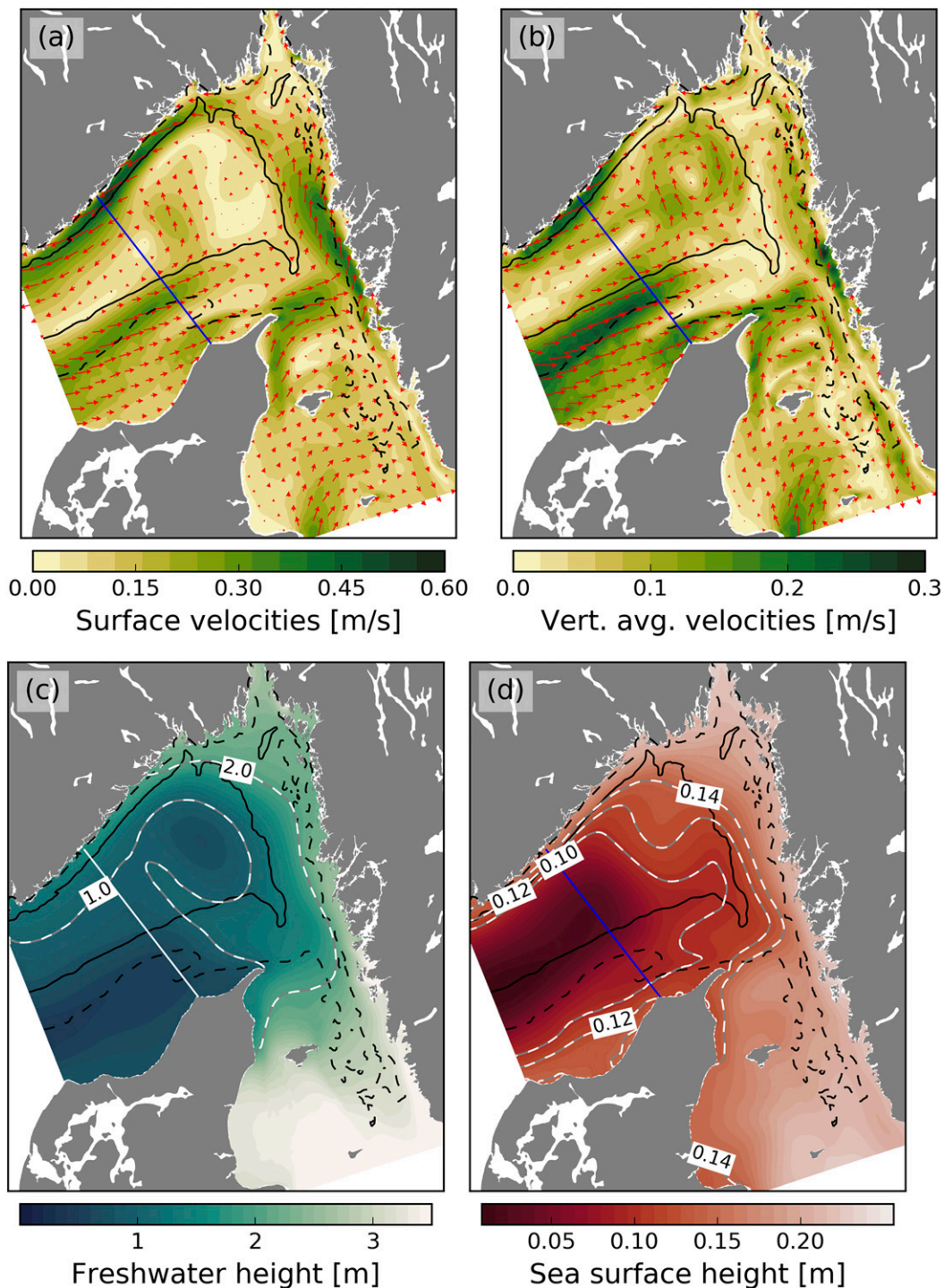


FIG. 6. Maps of (a) surface velocities, (b) vertically averaged velocities, (c) freshwater height, and (d) sea surface height averaged over the period 1 Nov 2014 to 31 Oct 2015. Additional white-dashed isolines are shown in (c) and (d) for emphasis. The black isolines denote the 200- (solid) and 50-m isobaths (dashed).

before and after the assimilation procedure. The impacts of the observations on the NCC transport through the data assimilation system can be obtained from the

analysis equation. In the case of ROMS-4DVAR, the total state vector \mathbf{x} containing all dependent variables is updated according to

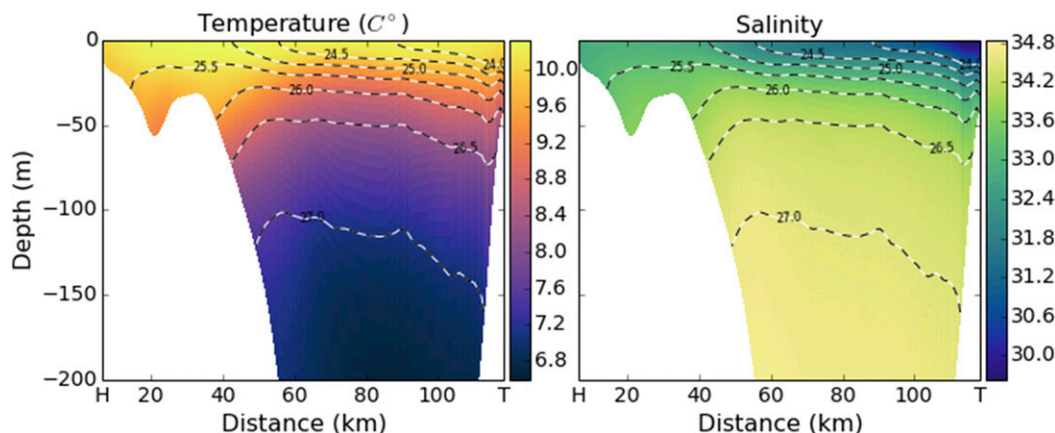


FIG. 7. Temperature and salinity in the section between Torungen (T) and Hirtshals (H) averaged over the period 1 Nov 2014 to 31 Oct 2015. The dashed lines show the density ($\sigma\text{-}t$) values.

$$\mathbf{x}_a = \mathbf{x}_b + \tilde{\mathbf{K}}[\mathbf{y} - G(\mathbf{x}_b)], \quad (4)$$

where the subscripts a and b denote analysis and background, respectively; \mathbf{y} is a vector containing the observations; G is an observation operator mapping from model to observation space; and $\tilde{\mathbf{K}}$ is the so-called practical gain matrix. If we define a scalar cost function $I(\mathbf{x})$, in our case the NCC transport across the Torungen–Hirtshals section, it is possible to obtain the unique contribution from each observation to the increment $\Delta I = I(\mathbf{x}_a) - I(\mathbf{x}_b)$, using the following expression [for more details, see, e.g., Moore et al. (2011b) and Neveu et al. (2016)]:

$$\Delta I = \mathbf{d}^T \tilde{\mathbf{K}}^T (\partial I / \partial \mathbf{x})|_{\mathbf{x}_b}, \quad (5)$$

where $\mathbf{d} = \mathbf{y} - G(\mathbf{x}_b)$ is the innovation vector. By choosing only a subset of the observations in \mathbf{d} and evaluating ΔI according to (5), we can quantify both the total impact of all the observations from a specific observation network (e.g., HF radar or satellite SST) and also calculate the average impact of every observation obtained from a specific observation network (referred to as increment per datum below).

Figure 3 shows the observation count and the analysis increments in the NCC transport for all assimilation cycles in April and October 2015, respectively. The bottom panels show that the total number of observations vary greatly from one assimilation cycle to the next. The bulk of the observations are satellite SST, but the HF radars provide a substantial amount of data as well. In situ data are primarily from regular monitoring cruises and FerryBox in addition to the observations received every day from the mooring mentioned above. The top panels of Fig. 3 show the analysis increments in the NCC transport through the

part of the Torungen–Hirtshals section shown below in Fig. 8. We note that the increments are both positive and negative, indicating that the transport estimates are not significantly biased, and that the analysis scheme adjusts the estimates either way depending on the specific conditions and the available observations. The middle panels show the average increment per datum (absolute value), and here we see that although the number of in situ observations is generally small, the value of a single in situ observation is generally large compared to a single SST or HF radar observation.

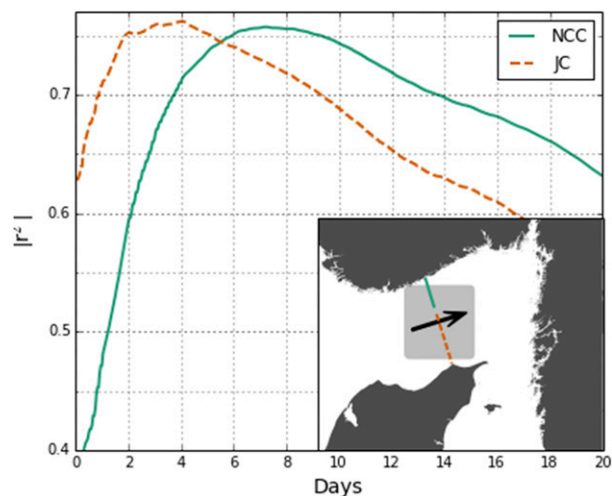


FIG. 8. Correlation between the time-integrated wind forcing [(1)] and the JC (dashed) and NCC (solid) transports as a function of integration period T . The inset shows the lateral extents of the Torungen–Hirtshals section used in the calculation of each transport as well as the area over which the wind forcing is averaged. The arrow points in what we here define as the positive direction.

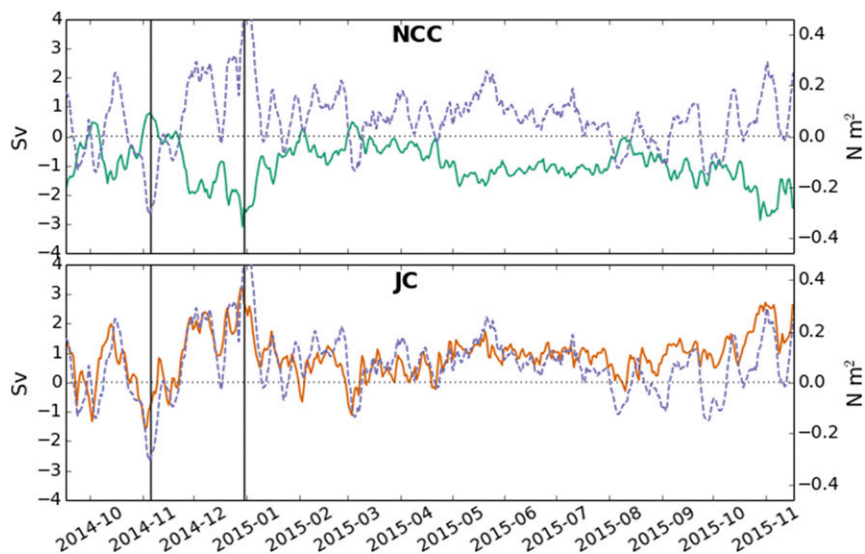


FIG. 9. Time series of the JC and NCC transports (solid) and the time-integrated wind forcing [(1)] for an integration period $T = 7$ days (dashed). The two vertical black lines denote a minimum and a maximum in the NCC transport and correspond to the two cases studied in more detail.

Figure 4 shows the average HF radar currents for the period 1 April to 26 October 2015 and also the average observation error. The equivalent model average for the same period is also shown, and the agreement is generally good except in the far range where the observation errors are large. The HF radar coverage area is quite some distance from the Torungen–Hirtshals section and hence the currents here are not observed directly. The high impact of the HF radar observations shown in the top panels of Fig. 3 thus point to a significant indirect influence through multivariate adjustments of the upstream conditions. These adjustments will necessarily have to be close enough to the section to influence the transport within the 24-h assimilation window. The distance to the HF radar coverage area is about 70–80 km, which suggests that the main impact is through adjustments of the fast barotropic mode. Another alternative is a baroclinic signal propagating directly from the coverage area across the isobaths to the section (assuming a propagation speed of about 1 m s^{-1}). We have calculated the average analysis increments in the barotropic speed for the period 1 April to 31 October 2015 (Fig. 5). This average shows that the largest increments are found north of Skagen and along the Swedish coast, with smaller increments along the Norwegian coast of $3\text{--}5 \text{ cm s}^{-1}$, which might explain the high impact of assimilating HF radar data. Dedicated data denial or observation sensitivity experiments have not yet been made, and the details of this upstream influence and the isolated

impact of the various observation platforms are presently unknown.

c. Annual averages in velocities, freshwater distribution, and sea surface height

Figure 6 shows maps of average surface velocities, vertically averaged velocities, freshwater height, and sea surface height for the period 1 November 2014 to 31 October 2015. Figure 6a shows that the strongest surface velocities are associated with the JC and the NCC and also with the current flowing northward along the Swedish coast. The circulation in the Kattegat is primarily anticyclonic in agreement with previous studies (e.g., Nielsen 2005). Interestingly, there is an average flow from the Danish to Norwegian side of the Skagerrak that crosses the deep Norwegian Trench. The average surface currents in the Skagerrak are often assumed to follow the coastlines, but it has been noted that the currents northeast of Skagen are comparatively weak and more variable (Rodhe 1996). It should also be emphasized that we only consider one specific year here and that our averages are not necessarily representative for longer periods.

In Fig. 6b we see that the vertically averaged currents have a similar pattern as the surface currents. There is evidence, however, of a persistent anticyclonic eddy at the northeastern end of the Norwegian Trench. This eddy is also visible in the freshwater height (Fig. 6c) as a pool of surface water with higher salinity and to some extent in the sea surface height (Fig. 6d) as a slight increase in the

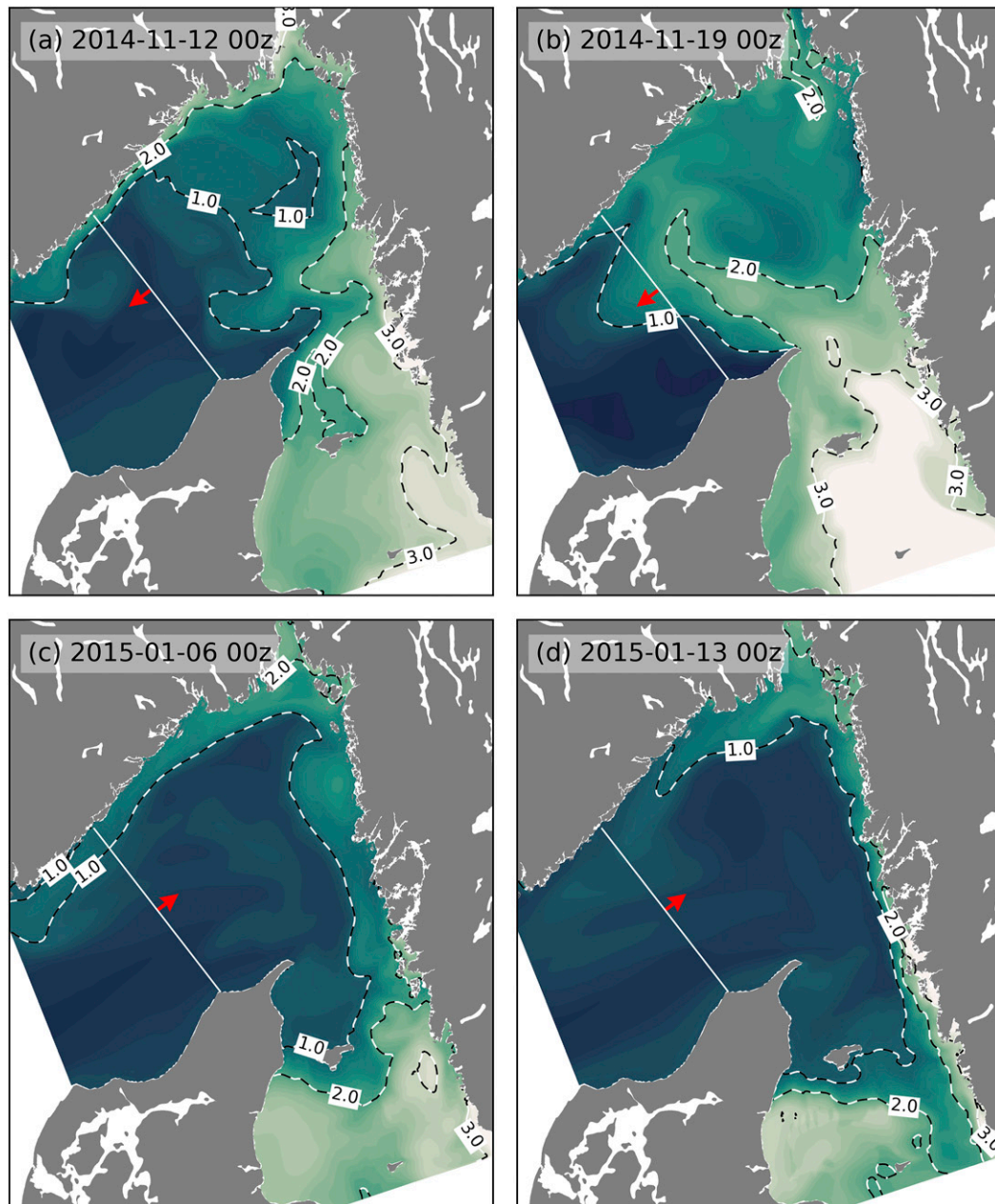


FIG. 10. Freshwater height (a) the week before and (b) at the time of the NCC minimum and (c) the week before and (d) at the NCC maximum. The red arrows indicate the dominating wind direction for each case.

surface level not following the isobaths. Such an eddy has previously been observed, for example, in satellite SAR images showing sea ice trapped in an eddy very much like the one depicted in Fig. 6b (see Hansen et al. 2010). We will briefly discuss mechanisms for generating and maintaining such anticyclonic circulation in section 4e.

Otherwise, the distribution of freshwater is as expected, with the freshwater content increasing gradually from the North Sea toward the Baltic Sea and

with more freshwater associated with transport of Baltic Sea Water in the NCC compared to the more saline JC coming in from the North Sea. The average sea surface height also increases gradually from the North Sea toward the Baltic Sea and reflects the dominating cyclonic circulation in the Skagerrak with a minimum in the deepest part. The average temperature and salinity in the upper 200m of the Torungen–Hirtshals section is shown in Fig. 7. Here,

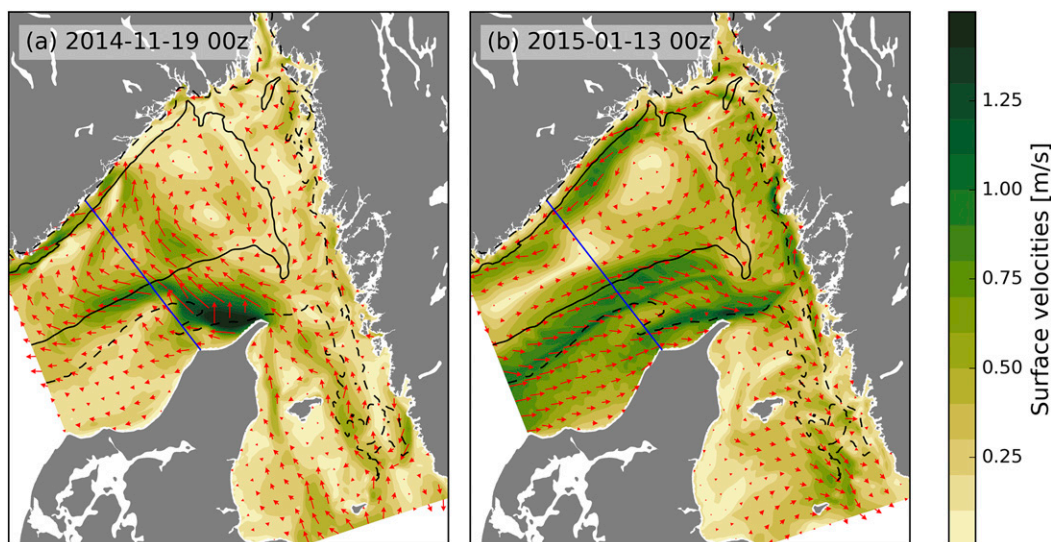


FIG. 11. Surface velocities at the time of the (a) NCC minimum and (b) NCC maximum. The black isolines denote the 200- (solid) and 50-m isobaths (dashed).

we also see that the lighter water masses are found close to either coast and that the salinities are lower toward the Norwegian side. The “doming” of the isotherms in the central Skagerrak noted in previous studies is also well reproduced in the annual average (e.g., [Pingree et al. 1982](#); [Danielssen et al. 1996](#); [Røed and Albretsen 2007](#)).

d. Correlations between the local wind forcing and the coastal transports

[Figure 8](#) shows the correlations between the time-integrated wind stress [(1)] and the JC and NCC transports through the Torungen–Hirtshals section for a range of integration periods T . The correlations increase sharply from T close to zero until attaining their maxima at $T \approx 4$ days and $T \approx 7$ days for the JC and NCC transports, respectively. As the integration period is further increased the correlations decrease slowly. A response time of 7 days for the NCC is in agreement with [Gustafsson \(1999\)](#), who based his estimate on a baroclinic propagation speed of 1 m s^{-1} . It is also interesting to note that this response time is close to the relaxation time scale of 8 days found by [Austin and Barth \(2002\)](#) for the correlation between alongshore winds and upwelling at the coast of Oregon. Whatever causes the particular response times in our case, it is clear that the time-integrated local wind forcing explains about 75% of the variance NCC transport, which may be considered one of the main results of this paper. At this point we should mention that we also calculated the correlation between the transports and

wind stress across the basin, that is, in the direction from Hirtshals toward Torungen. The correlations are low, however, with values in the range -0.2 to 0 for both the NCC and the JC, and they do not possess such clear peaks. These results are therefore not shown, and in the following we only consider the component of the wind stress into or out of the Skagerrak as indicated in [Fig. 8](#).

[Figure 9](#) shows time series of the time-integrated wind stress and JC and NCC transports using $T = 7$ days. The direction is defined as in [Fig. 8](#), that is, the NCC transport is on average negative while the JC transport is on average positive, and a positive wind stress is produced by winds into the Skagerrak. The time series show that the largest variations are in the cold season and the fluctuations are small from late spring through summer. [Gustafsson \(1997\)](#), see also references therein) describes how winds into the Skagerrak will lead to upwelling along the Norwegian coast, with a reduction in available potential energy and hence a reduction in the NCC. At the same time the Ekman transport across the Skagerrak will lead to an intensification of the JC. This intensification then propagates along the rim of the Skagerrak and after some time the NCC transport should increase again. A shift in the wind direction from southwesterly to northeasterly during this period will further strengthen the NCC transport out of the Skagerrak. Our results show that the intensification of the JC peaks after 4 days of sustained winds into the Skagerrak and that the intensification of the NCC lags the JC with an additional 3 days. The distance between Hirtshals and Torungen, measured

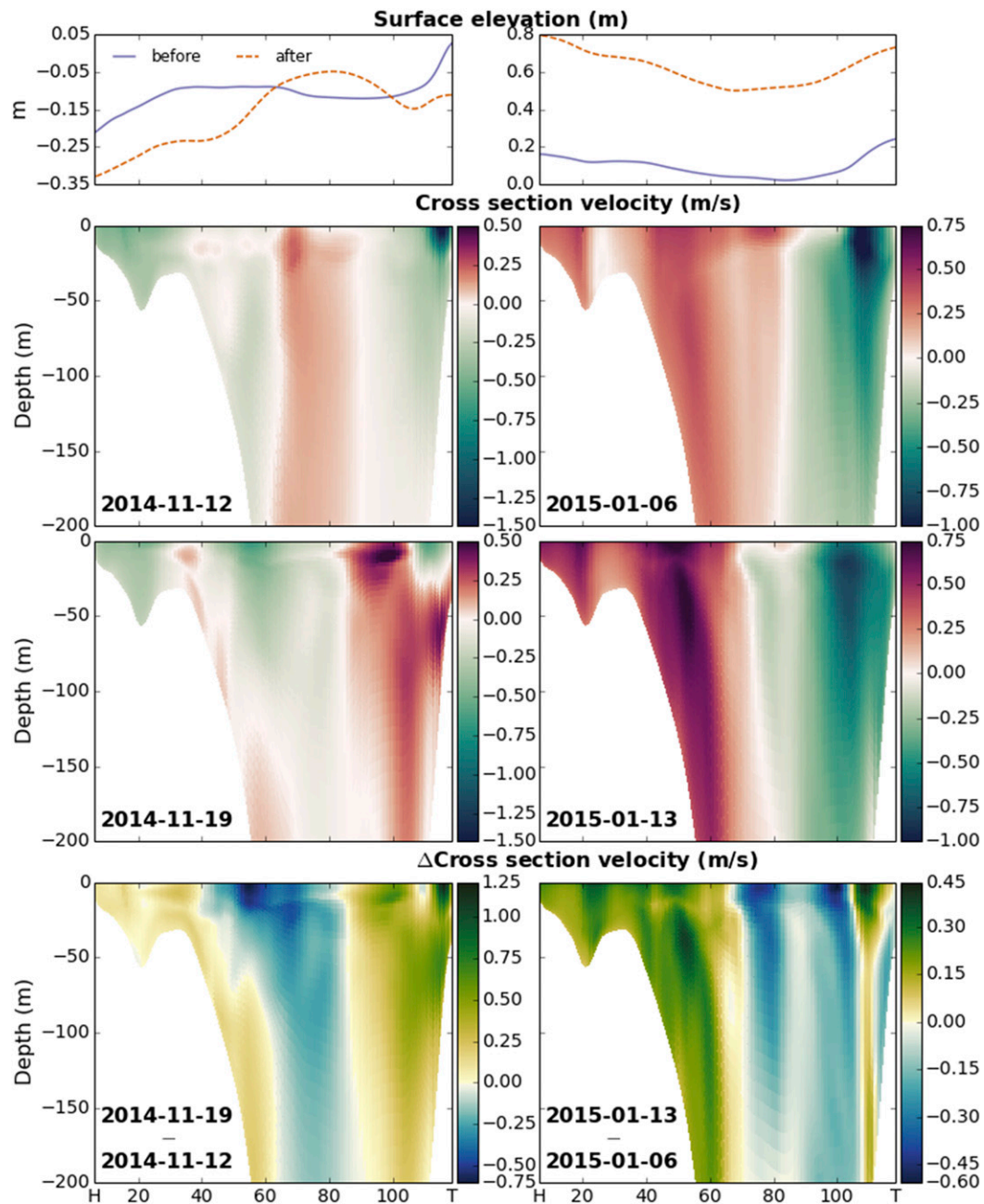


FIG. 12. Velocities across the Torungen–Hirtshals section for the case of the NCC (left) minimum and (right) maximum. (top) The surface elevation one week prior (solid) and at the time of the minimum/maximum (dashed). (bottom) The differences in velocity that develop in the week leading up to the NCC minimum/maximum.

along the coast in a counterclockwise direction, is approximately 300 km, which indicates a propagation speed of about 1.2 m s^{-1} .

e. Mechanisms connecting the local wind forcing and the transport

We now proceed to investigate two cases in more detail. The two vertical black lines in Fig. 9 mark (i) a

minimum (in fact a reversal) and (ii) a maximum in the NCC, and we will refer to these situations as case 1 and case 2, respectively. Figure 10 shows maps of the fresh-water height at these extremes as well as the situations one week before, consistent with our finding of a response time of 7 days for the NCC to the wind forcing. Figure 11 shows the surface velocities for the two extremes.

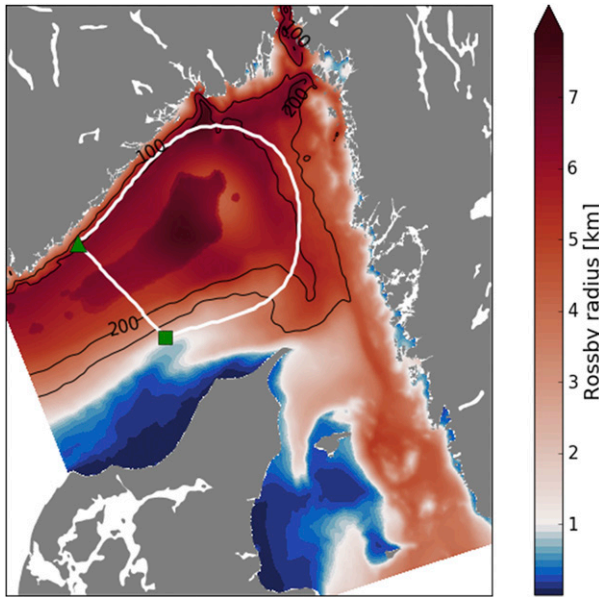


FIG. 13. Rossby radius of deformation for the first baroclinic mode (annual average), estimated using the method of Chelton et al. (1998). The black lines denote the 100- and 200-m isobaths. The white lines indicate the paths along which the profile potential energy is evaluated for Fig. 14. Both paths start at the position of the square and end at the position of the triangle.

The case with winds out of the Skagerrak and a minimum in the NCC is shown in Figs. 10a and 10b and in Fig. 11a. We see that the Kattegat–Skagerrak Front initially passes from Skagen toward the Swedish coast, and there is slightly more freshwater in the surface layer north of the front as compared to the annual average (Fig. 6). At the time of the minimum in the NCC, the JC is blocked and the Kattegat–Skagerrak Front now crosses over toward the Norwegian coast [for a description of a similar case, see Aure et al. (2007)]. Here, a tongue of fresher water turns east; interacting with the more saline water masses to the east and forming an anticyclonic eddy (cf. Fig. 11a).

In the case with winds into the Skagerrak and a maximum in the NCC, there is initially much less freshwater in the Skagerrak (Fig. 11c). Now the Kattegat–Skagerrak Front is pushed back into the Kattegat, and eventually we find saline surface water all the way toward the southern boundary in the Kattegat. A local minimum in the freshwater height appears in approximately the same position as the local minimum in the annual average, coinciding with the location of the anticyclonic eddy in case 1. The circulation in this case is, however, cyclonic (Fig. 11b).

Figure 12 shows the velocities through the Torungen–Hirtshals section at the peaks and one week before. The case with winds out of the Skagerrak and a blocking of the coastal currents (left-hand side panels) is dominated by the Kattegat–Skagerrak Front, which crosses the section twice. At the point in time when we have a minimum in the coastal currents, the sea surface height has a local maximum in the interior of the Skagerrak associated with the presence of freshwater from the Kattegat. The case with winds into the Skagerrak and intensification of the coastal currents (right-hand side panels) is easier to explain in terms of Ekman transport and upwelling: sharp gradients in the density field on the Norwegian side are reduced because of upwelling (not shown here), and the sea surface slope toward the Danish side increases as the surface water is transported toward Denmark, leading to an intensification of the JC. From the bottom panel on the right we do see that the part of the NCC closest to the coast decrease in strength, but an increase in the interior parts implies an overall strengthening of the total transport on the Norwegian side of the basin. It is also clear that there is a net inflow to the Skagerrak with an overall increase in the surface level.

We now proceed to investigate whether we can track a signal around the rim of the Skagerrak Basin. Figure 13 shows the Rossby radius of deformation for the first baroclinic mode, estimated using the WKB approximation of Chelton et al. (1998). This approximation is known to yield too low values, in particular in shallow areas (Nurser and Bacon 2014; Osinski et al. 2010). Here, we only conclude that the Rossby radius on the Danish side increases quite rapidly out from the 100-m isobath, and the strongest indication of signal propagation is found here and not closer to the Danish coast. Of the various parameters calculated from the model output, it is the profile potential energy [(3)] that provides the clearest signal. Figure 14 contains Hovmöller diagrams of the profile potential energy along the paths shown in Fig. 13 for the two cases. The choice of path around the basin is guided by the values for the average Rossby radius, and varying the path somewhat gives qualitatively the same results.

We see that in case 1 we can track changes in the profile potential energy both across the Skagerrak and along the coast in a clockwise direction, which is consistent with advection of Baltic Water in the Kattegat–Skagerrak Front and the generation of an anticyclonic eddy. In case 2, however, there is no clear indication of a signal propagating across the Skagerrak, but we

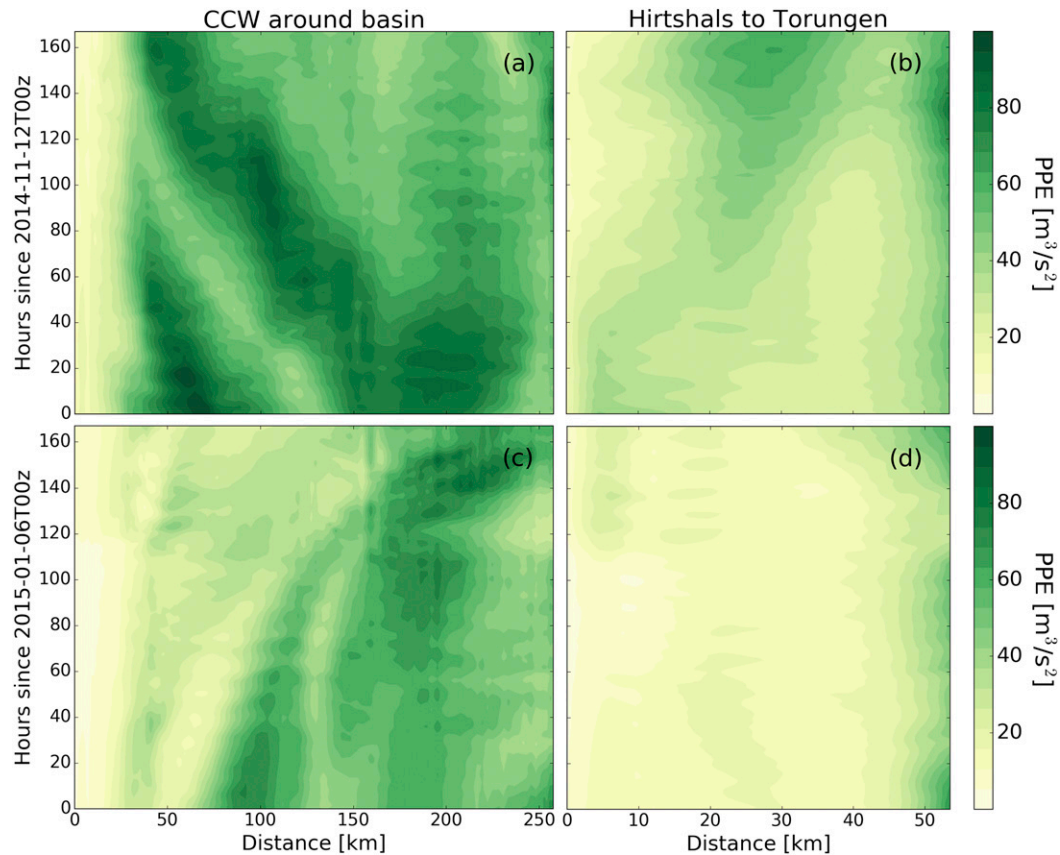


FIG. 14. Hovmöller diagrams for the profile potential energy (PPE) for (top) case 1 and (bottom) case 2.

can track changes in the profile potential energy in a counterclockwise direction along the coast. The phase speed is not constant but increases from about 0.15 to about 0.6 m s^{-1} along the steep slopes on the Norwegian side. These values are much smaller than the propagation speeds estimated in, for example, [Gustafsson \(1997\)](#). We may also note that the signal originates about $70\text{--}80$ km east of Hirtshals, closer to the Swedish coast.

5. Discussion and concluding remarks

Numerous authors have commented on the large variability in the Kattegat and Skagerrak circulation, and several conceptual models for how this circulation depends on local and remote atmospheric forcing has been presented in the literature (e.g., [Stigebrandt 1983](#); [Gustafsson 1997](#); [Nielsen 2005](#)). Our approach has been to use a high-resolution reanalysis assimilating all available in situ and remote sensing observations of salinity and temperature. In addition, we have assimilated surface currents from two coastal HF radars that

were ideally placed to observe the exchange between the Kattegat and Skagerrak. We can investigate details of the circulation in our analyzed fields that are missing in datasets from large field campaigns. Such modeling effort is costly in terms of computing resources, and we have only covered a period of slightly more than 1 year. Therefore, we do not know if our results are representative of the circulation on longer time scales, but note that the model bias and RMSE values are small and that annual averages reproduce the main features of the circulation as reported in previous studies, such as an anticyclonic surface flow in the Kattegat, an overall cyclonic circulation in the Skagerrak, and realistic stratification across the Torungen–Hirtshals section.

When investigating the relation between the time-integrated wind forcing in the Skagerrak and the strength of the coastal currents, we find remarkably high correlations. The Norwegian Coastal Current has a response time to the local wind forcing of about 7 days, in agreement with previous estimates ([Gustafsson 1999](#)). The two cases studied more in

detail in section 4e suggest an asymmetry in the forcing mechanisms. For winds into the Skagerrak, if the Kattegat–Skagerrak Front is either in its normal position between Skagen and the Swedish coast, or located even farther south, the direct influence of the Baltic Sea outflow will be small. In such cases the conceptual models presented in earlier studies could be valid. For winds out of the Skagerrak, a strong outflow of Baltic Sea Water from the Kattegat can disrupt local processes near the coasts on either side. If the Kattegat–Skagerrak Front crosses over toward the Norwegian coast, both the JC and NCC will be blocked, in particular if such situations tend to induce an anticyclonic eddy at the northeastern end of the Norwegian Trench. From our results it appears that this anticyclonic eddy is a common feature meriting further investigation. In addition, there is an asymmetry in the barotropic response to wind forcing. The Skagerrak is open to the west and there are no physical barriers blocking a surge from the North Sea. In contrast, winds out of Skagerrak will initially lead to a decrease in the sea surface level here, which will again trigger a more complex response in the Kattegat and in the flows through the narrow straits toward the Baltic farther south (e.g., Stigebrandt 1983; Nielsen 2005). Despite these asymmetries in the forcing mechanisms, the time series of the transport and the history of the local winds (Fig. 9) indicate that the coastal currents respond just as strongly to winds out of the Skagerrak as into the Skagerrak.

Acknowledgments. We express our thanks to Anders Stigebrandt (University of Gothenburg) and Andrew Moore (UCSC) for stimulating discussions and to Pia Andersson, Johan Kronsell, and Magnus Wenzer at the SMHI for generously sharing the HF radar data. Financial support from the Research Council of Norway (Grants 244262 RETROSPECT and 237906 CIRFA), and the Swedish Research Council Formas (Grant “Microplastics in marine waters: Sources, pathways, fate and indicator species”) is gratefully acknowledged. High-performance computing resources have been provided by NOTUR (NN9197K).

REFERENCES

- Albretsen, J., J. Aure, R. Saetre, and D. S. Danielssen, 2012: Climatic variability in the Skagerrak and coastal waters of Norway. *ICES J. Mar. Sci.*, **69**, 758–763, <https://doi.org/10.1093/icesjms/fsr187>.
- Austin, J. A., and J. A. Barth, 2002: Variation in the position of the upwelling front on the Oregon shelf. *J. Geophys. Res.*, **107**, 3180, doi:10.1029/2001JC000858.
- Berntsen, J., and E. Svendsen, 1999: Using the SKAGEX dataset for evaluation of ocean model skills. *J. Mar. Syst.*, **18**, 313–331, [https://doi.org/10.1016/S0924-7963\(97\)00111-5](https://doi.org/10.1016/S0924-7963(97)00111-5).
- Broquet, G., C. A. Edwards, A. M. Moore, B. S. Powell, M. Veneziani, and J. D. Doyle, 2009: Application of 4D-variational data assimilation to the California Current System. *Dyn. Atmos. Oceans*, **48**, 69–92, <https://doi.org/10.1016/j.dynatmoce.2009.03.001>.
- Broström, G., A. Carrasco, L. R. Hole, S. Dick, F. Janssen, J. Mattsson, and S. Berger, 2011: Usefulness of high resolution coastal models for operational oil spill forecast: The “Full City” accident. *Ocean Sci.*, **7**, 805–820, <https://doi.org/10.5194/os-7-805-2011>.
- Chapman, R. D., and H. C. Graber, 1997: Validation of HF radar measurements. *Oceanography*, **10** (2), 76–79, <https://doi.org/10.5670/oceanog.1997.28>.
- Chelton, D. B., R. A. Deszoeke, M. G. Schlax, K. El Naggar, and N. Siwertz, 1998: Geographical variability of the first baroclinic Rossby radius of deformation. *J. Phys. Oceanogr.*, **28**, 433–460, [https://doi.org/10.1175/1520-0485\(1998\)028<0433:GVOTFB>2.0.CO;2](https://doi.org/10.1175/1520-0485(1998)028<0433:GVOTFB>2.0.CO;2).
- Craig, P. D., and M. L. Banner, 1994: Modeling wave-enhanced turbulence in the ocean surface layer. *J. Phys. Oceanogr.*, **24**, 2546–2559, [https://doi.org/10.1175/1520-0485\(1994\)024<2546:MWETIT>2.0.CO;2](https://doi.org/10.1175/1520-0485(1994)024<2546:MWETIT>2.0.CO;2).
- Danielssen, D. S., E. Svendsen, and M. Ostrowski, 1996: Long-term hydrographic variation in the Skagerrak based on the section Torungen–Hirtshals. *ICES J. Mar. Sci.*, **53**, 917–925, <https://doi.org/10.1006/jmsc.1996.0113>.
- , L. Edler, S. Fonselius, L. Hernroth, M. Ostrowski, E. Svendsen, and L. Talpsepp, 1997: Oceanographic variability in the Skagerrak and northern Kattegat, May–June, 1990. *ICES J. Mar. Sci.*, **54**, 753–773, <https://doi.org/10.1006/jmsc.1996.0210>.
- Dooley, H. D., 1974: Hypotheses concerning the circulation of the northern North Sea. *ICES J. Mar. Sci.*, **36**, 54–61, <https://doi.org/10.1093/icesjms/36.1.54>.
- Eastwood, S., 2011: Atlantic high latitude L3 sea surface temperature product user manual. Norwegian Meteorological Institute Tech. Rep., 33 pp.
- Egbert, G. D., and S. Y. Erofeeva, 2002: Efficient inverse modeling of barotropic ocean tides. *J. Atmos. Oceanic Technol.*, **19**, 183–204, [https://doi.org/10.1175/1520-0426\(2002\)019<0183:EIMOBO>2.0.CO;2](https://doi.org/10.1175/1520-0426(2002)019<0183:EIMOBO>2.0.CO;2).
- Fairall, C. W., E. F. Bradley, J. E. Hare, A. A. Grachev, and J. B. Edson, 2003: Bulk parameterization of air–sea fluxes: Updates and verification for the COARE algorithm. *J. Climate*, **16**, 571–591, [https://doi.org/10.1175/1520-0442\(2003\)016<0571:BPOASF>2.0.CO;2](https://doi.org/10.1175/1520-0442(2003)016<0571:BPOASF>2.0.CO;2).
- Golbeck, I., and Coauthors, 2015: Uncertainty estimation for operational ocean forecast products—A multi-model ensemble for the North Sea and the Baltic Sea. *Ocean Dyn.*, **65**, 1603–1631, <https://doi.org/10.1007/s10236-015-0897-8>.
- Good, S. A., M. J. Martin, and N. A. Rayner, 2013: EN4: Quality controlled ocean temperature and salinity profiles and monthly objective analyses with uncertainty estimates. *J. Geophys. Res. Oceans*, **118**, 6704–6716, <https://doi.org/10.1002/2013JC009067>.
- Gratton, S., and J. Tshimanga, 2009: An observation-space formulation of variational assimilation using a restricted preconditioned conjugate gradient algorithm. *Quart. J. Roy. Meteor. Soc.*, **135**, 1573–1585, <https://doi.org/10.1002/qj.477>.
- Gustafsson, B., 1997: Interaction between Baltic Sea and North Sea. *Dtsch. Hydrogr. Z.*, **49**, 165–183, <https://doi.org/10.1007/BF02764031>.
- , 1999: High frequency variability of the surface layers in the Skagerrak during SKAGEX. *Cont. Shelf Res.*, **19**, 1021–1047, [https://doi.org/10.1016/S0278-4343\(99\)00008-4](https://doi.org/10.1016/S0278-4343(99)00008-4).
- , and A. Stigebrandt, 1996: Dynamics of the freshwater-influenced surface layers in the Skagerrak. *J. Sea Res.*, **35**, 39–53, [https://doi.org/10.1016/S1385-1101\(96\)90733-9](https://doi.org/10.1016/S1385-1101(96)90733-9).

- Haller, M., F. Janssen, J. Siddorn, W. Petersen, and S. Dick, 2015: Evaluation of numerical models by FerryBox and fixed platform in situ data in the southern North Sea. *Ocean Sci.*, **11**, 879–896, <https://doi.org/10.5194/os-11-879-2015>.
- Hansen, M., K. Kloster, K.-F. Dagestad, S. Sandven, and J. Johannessen, 2010: Retrieval of sea ice drift from SAR Doppler shift. *Proc. ESA Living Planet Symp.*, Bergen, Norway, ESA, <https://www.nersc.no/biblio/retrieval-sea-ice-drift-sar-doppler-shift>.
- Jakobsen, F., 1997: Hydrographic investigation of the northern Kattegat Front. *Cont. Shelf Res.*, **17**, 533–554, [https://doi.org/10.1016/S0278-4343\(96\)00044-1](https://doi.org/10.1016/S0278-4343(96)00044-1).
- Marchesiello, P., J. C. McWilliams, and A. Shchepetkin, 2001: Open boundary conditions for long-term integration of regional oceanic models. *Ocean Modell.*, **3**, 1–20, [https://doi.org/10.1016/S1463-5003\(00\)00013-5](https://doi.org/10.1016/S1463-5003(00)00013-5).
- McClimans, T., J. Pietrzak, V. Huess, N. Kliem, J. Nilsen, and B. Johannessen, 2000: Laboratory and numerical simulation of the Skagerrak circulation. *Cont. Shelf Res.*, **20**, 941–974, [https://doi.org/10.1016/S0278-4343\(00\)00007-8](https://doi.org/10.1016/S0278-4343(00)00007-8).
- Moore, A. M., H. G. Arango, G. Broquet, B. S. Powell, A. T. Weaver, and J. Zavala-Garay, 2011a: The Regional Ocean Modeling System (ROMS) 4-dimensional variational data assimilation systems. *Prog. Oceanogr.*, **91**, 34–49, <https://doi.org/10.1016/j.pocean.2011.05.004>.
- , and Coauthors, 2011b: The Regional Ocean Modeling System (ROMS) 4-dimensional variational data assimilation systems. *Prog. Oceanogr.*, **91**, 50–73, <https://doi.org/10.1016/j.pocean.2011.05.003>.
- , and Coauthors, 2011c: The Regional Ocean Modeling System (ROMS) 4-dimensional variational data assimilation systems. *Prog. Oceanogr.*, **91**, 74–94, <https://doi.org/10.1016/j.pocean.2011.05.005>.
- Neveu, E., A. M. Moore, C. A. Edwards, J. Fiechter, P. Drake, W. J. Crawford, M. G. Jacox, and E. Nuss, 2016: An historical analysis of the California Current circulation using ROMS 4D-Var: System configuration and diagnostics. *Ocean Modell.*, **99**, 133–151, <https://doi.org/10.1016/j.ocemod.2015.11.012>.
- Nielsen, M. H., 2005: The baroclinic surface currents in the Kattegat. *J. Mar. Syst.*, **55**, 97–121, <https://doi.org/10.1016/j.jmarsys.2004.08.004>.
- Nurser, A., and S. Bacon, 2014: The Rossby radius in the Arctic Ocean. *Ocean Sci.*, **10**, 967–975, <https://doi.org/10.5194/os-10-967-2014>.
- Osinski, R., D. Rak, W. Walczowski, and J. Piechura, 2010: Baroclinic Rossby radius of deformation in the southern Baltic Sea. *Oceanologia*, **52**, 417–429, <https://doi.org/10.5697/oc.52.3.417>.
- Pingree, R. D., P. M. Holligan, G. T. Mardell, and R. P. Harris, 1982: Vertical distribution of plankton in the Skagerrak in relation to doming of the seasonal thermocline. *Cont. Shelf Res.*, **1**, 209–219, [https://doi.org/10.1016/0278-4343\(82\)90005-X](https://doi.org/10.1016/0278-4343(82)90005-X).
- Rodhe, J., 1996: On the dynamics of the large-scale circulation of the Skagerrak. *J. Sea Res.*, **35**, 9–21, [https://doi.org/10.1016/S1385-1101\(96\)90731-5](https://doi.org/10.1016/S1385-1101(96)90731-5).
- Røed, L. P., and J. Albretsen, 2007: The impact of freshwater discharges on the ocean circulation in the Skagerrak/northern North Sea area. Part I: Model validation. *Ocean Dyn.*, **57**, 269–285, <https://doi.org/10.1007/s10236-007-0122-5>.
- Röhrs, J., A. K. Sperrevik, K. H. Christensen, G. Broström, and Ø. Breivik, 2015: Comparison of HF radar measurements with Eulerian and Lagrangian surface currents. *Ocean Dyn.*, **65**, 679–690, <https://doi.org/10.1007/s10236-015-0828-8>.
- Saetre, R., Ed., 2007: *The Norwegian Coastal Current: Oceanography and Climate*. Tapir Academic Press, 159 pp.
- Shchepetkin, A. F., and J. C. McWilliams, 2005: The Regional Oceanic Modeling System (ROMS): A split-explicit, free-surface, topography-following-coordinate oceanic model. *Ocean Modell.*, **9**, 347–404, <https://doi.org/10.1016/j.ocemod.2004.08.002>.
- , and —, 2009: Computational kernel algorithms for fine-scale, multiprocess, longtime oceanic simulations. *Computational Methods for the Atmosphere and the Oceans*, P. Ciarlet, Ed., Vol. 14, *Handbook of Numerical Analysis*, Elsevier, 121–183.
- Stigebrandt, A., 1983: A model for the exchange of water and salt between the Baltic and the Skagerrak. *J. Phys. Oceanogr.*, **13**, 411–427, [https://doi.org/10.1175/1520-0485\(1983\)013<0411:AMFTEO>2.0.CO;2](https://doi.org/10.1175/1520-0485(1983)013<0411:AMFTEO>2.0.CO;2).
- , 1987: Computations of the flow of dense water into the Baltic Sea from hydrographical measurements in the Arkona Basin. *Tellus*, **39A**, 170–177, <https://doi.org/10.1111/j.1600-0870.1987.tb00298.x>.
- Umlauf, L., H. Burchard, and K. Hutter, 2003: Extending the $k-\omega$ turbulence model towards oceanic applications. *Ocean Modell.*, **5**, 195–218, [https://doi.org/10.1016/S1463-5003\(02\)00039-2](https://doi.org/10.1016/S1463-5003(02)00039-2).
- Warner, J. C., C. R. Sherwood, H. G. Arango, and R. P. Signell, 2005: Performance of four turbulence closure models implemented using a generic length scale method. *Ocean Modell.*, **8**, 81–113, <https://doi.org/10.1016/j.ocemod.2003.12.003>.
- Weaver, A., and P. Courtier, 2001: Correlation modelling on the sphere using a generalized diffusion equation. *Quart. J. Roy. Meteor. Soc.*, **127**, 1815–1846, <https://doi.org/10.1002/qj.49712757518>.